Heat transfer and wall temperature effects in shock-wave/turbulent boundary layer interactions

M. Bernardini,[1, *] I. Asproulias,[1] J. Larsson,[2] S. Pirozzoli,[1] and F. Grasso[3]

[1]*Dipartimento di Ingegneria Meccanica e Aerospaziale,*

Università di Roma 'La Sapienza' Via Eudossiana 18, 00184 Roma, Italia

[2]*Dept. of Mechanical Engineering, University of Maryland, College Park, MD 20742*

[3]*Cnam-Laboratoire DynFluid, 151 Boulevard de L'Hopital, 75013 Paris*

(Dated: March 10, 2017)

Abstract

Direct numerical simulations are carried out to investigate the effect of the wall temperature on the behavior of oblique shock-wave/turbulent boundary layer interactions at freestream Mach number 2.28 and shock angle of the wedge generator $\varphi = 8°$. Five values of the wall-to-recovery-temperature ratio (T_w/T_r) are considered, corresponding to cold, adiabatic and hot wall thermal conditions. We show that the main effect of cooling is to decrease the characteristic scales of the interaction in terms of upstream influence and extent of the separation bubble. The opposite behavior is observed in the case of heating, which produces a marked dilatation of the interaction region. The distribution of the Stanton number shows that a strong amplification of the heat transfer occurs across the interaction, with the maximum thermal and dynamic loads found for the case of the cold wall. The analysis reveals that the fluctuating heat flux exhibits a strong intermittent behavior, characterized by scattered spots with extremely high values compared to the mean. Furthermore, the analogy between momentum and heat transfer, typical of compressible, wall-bounded, equilibrium turbulent flows, does not apply for most part of the interaction domain. The pre-multiplied spectra of the wall heat flux do not show any evidence of the influence of the low-frequency shock motion, and the primary mechanism for the generation of peak heating is found to be linked with the turbulence amplification in the interaction region.

----

[*] matteo.bernardini@uniroma1.it

I. INTRODUCTION

In a wide range of high-speed applications in the aerospace industry, shock-wave/turbulent boundary layer interactions (SBLI) have a large impact on the aerodynamic and thermodynamic design, with SBLI being responsible for increased internal machine losses, thermal and structural fatigue due to increased heat transfer rates and substantial modification of the wall-pressure signature, flow unsteadiness, shock/vortex interaction and broadband noise emission. Improving the understanding of these critical features is essential to enhance the capability to predict important quantities like the location and magnitude of peak heating, as well as for the development of effective flow control methods [1].

Most prior scientific work on SBLI, of both experimental [2–7] and numerical nature [8–15], has been aimed at the case of adiabatic wall conditions and much effort has been invested in the last decade to characterize the large-scale, low-frequency unsteadiness typically found in the interaction region. This phenomenon can be particularly severe when the shock is strong enough to produce separation of the incoming boundary layer [16].

The influence of wall thermal conditions on the characteristics of SBLI can be considerable and wall cooling is often advocated as a possible candidate for flow control. Strong cooling is capable of [17]: (i) shifting the laminar-turbulent boundary layer transition toward higher Reynolds numbers; (ii) producing a fuller incoming boundary layer velocity profile; and (iii) reducing the thickness of the subsonic layer by decreasing the local speed of sound. Unfortunately, only a few experimental studies have been conducted on this topic, all based on the analysis of mean flow properties.

The effects of heat transfer in turbulent interactions over a compression ramp have been investigated by Spaid and Frishett [18], who performed experiments at freestream Mach number $M_\infty = 2.9$, by considering a cold (wall-to-recovery-temperature ratio $T_w/T_r = .47$) and a nearly adiabatic wall ($T_w/T_r = 1.05$). Their results showed that the effect of wall cooling, relative to the adiabatic condition, is to increase the incipient separation angle and to decrease the separation distance. Similar conclusions were later reported by Back and Cuffel [19], who considered an oblique shock-wave impinging on a turbulent boundary layer at $M_\infty = 3.5$ with surface cooling ($T_w/T_r = .44$).

An in-depth experimental analysis of a shock reflection over a strongly heated wall ($T_w/T_r = 2$) was carried out by Delery [20], who considered a two-dimensional test ar-

rangement for an upstream Mach number $M_\infty = 2.4$ and two incident shock wave strengths. The experimental measurements showed that heating the surface greatly increases the extent of the interaction zone and the separation point moves much farther upstream than under adiabatic conditions. More recently, an investigation of the impact of wall temperature on a $M_\infty = 2.3$ shock-induced boundary layer separation has been carried out by Jaunet $et\ al.$ [21] for shock deflection angles ranging from 3.5^o to 9.5^o under adiabatic ($T_w/T_r = 1$) and wall heating conditions ($T_w/T_r = 1.4, 1.9$). Their extensive experimental analysis based on Schlieren visualizations, particle image velocimetry (PIV) and time-resolved hot-wire measurements highlighted that a hot wall leads to an increase of the interaction length-scales, which is mainly associated with changes of the wall incoming conditions. A slight influence was also observed on the onset of separation, shifted to smaller flow deviations in the heated case. This scale change due to wall thermal conditions has also an effect on the flow unsteadiness, the lower frequencies becoming more and more important by heating the wall.

Measurements of heat transfer in SBLI were first reported by Hayashi $et\ al.$ [22], who considered a $M_\infty = 4$ boundary layer developing over an isothermal cold wall ($T_w/T_r \approx 0.6$) interacting with an oblique shock at various incident angles. They observed a complex spatial variation of the heat transfer coefficient, characterized by a rapid increase near the separation point, followed by a sharp reduction within the separation bubble and a further increase in the proximity of the reattachment point. Combined measurements of skin friction and heat transfer have been recently reported by Schülein [23] who considered an impinging shock at $M_\infty = 5$ and three values of the incident angle. Their results show a strong increase of the heat flux in the separation zone, characterized by a complex non-equilibrium behavior, in which the Reynolds analogy between momentum and heat flux is not valid. A strong increase in the Reynolds analogy factor across the shock was also noticed by Evans and Smits [24], who reported measurements of the mean heat transfer in a shock-wave/turbulent boundary layer interaction generated by a $16°$ compression corner in a $M_\infty = 2.84$ flow.

A relatively large number of direct numerical and large-eddy simulations (DNS/LES) of both compression ramp and impinging shock interactions have appeared over the last decade [8, 11, 12, 25, 26]. However, all these studies addressed the case of adiabatic wall conditions and to our knowledge, no high-fidelity simulations have been carried out to explore the effect of neither wall heating nor cooling in SBLI. The main objective of the present work is to fill this gap by providing a numerical study on the influence of wall thermal conditions

on the behavior of oblique SBLI. The analysis is based on direct numerical simulations to explore the effect of different wall-to-recovery-temperature ratios. This can be beneficial for the improvement of current turbulence modeling for SBLI, in particular for the computation of the heat transfer, which is the most challenging aspect of these flows, and it is well known that numerical predictions based on the solution of Reynolds Averaged Navier-Stokes equations are rather poor [27, 28], with significant differences (up to 100%) among different turbulence models. A careful characterization of how the separation bubble, the skin friction and heat transfer are affected by the wall thermal conditions is a core objective of this work, and it represents the key stepping-stone towards harnessing wall cooling to stabilize and control SBLI.

The paper is organized as follows. After the introduction, the numerical strategy and the flow conditions of the simulations are described in Section 2. The main results are presented in Section 3, where we also provide a comparison with experimental data. The discussion first focuses on the modifications induced by the wall temperature on the structure of SBLI, both in terms of lenghtscales and turbulence amplification. Emphasis is then put on the heat transfer behavior across the interaction and for the first time fluctuating heat flux data are reported and analyzed. Conclusions are finally provided in Section 4.

II. COMPUTATIONAL SETUP

A. Flow solver

We solve the three-dimensional Navier-Stokes equations for a perfect compressible gas with Fourier heat law and Newtonian viscous terms. The molecular viscosity μ is assumed to depend on temperature T through Sutherland's law, and the thermal conductivity is computed as $k = c_p \mu / Pr$, the molecular Prandtl number being set to $Pr = 0.72$.

The Navier-Stokes equations are discretized on a Cartesian mesh and solved by means of an in-house finite-difference flow solver, extensively validated for wall-bounded flows and shock boundary layer interactions in the transonic and supersonic regime [29, 30]. The solver incorporates state-of-the-art numerical algorithms, specifically designed to cope with the challenging problems associated with the solution of high-speed turbulent flows, i.e. the need to accurately resolve a wide spectrum of turbulent scales and to capture steep gra-
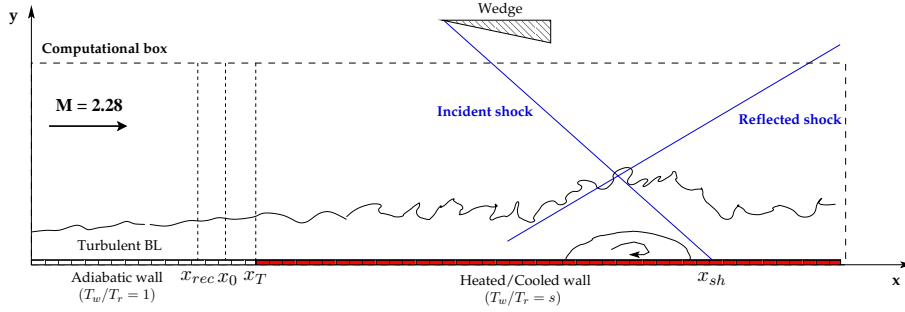
4

FIG. 1: Sketch of the flow configuration under investigation.

dients without undesirable numerical oscillations. In the current version of the code the convective terms are discretized by means of a hybrid conservative sixth-order central/fifth-order WENO scheme, with a switch based on the Ducros sensor [31]. To improve numerical stability, the triple splitting of the convective terms [32] is used in a locally conservative implementation [33]. The viscous terms are approximated with sixth-order central differences, after being expanded to Laplacian form to guarantee physical dissipation at the smallest scales resolved by the computational mesh. Time advancement is performed by means of a third-order, low-storage, explicit Runge-Kutta algorithm [34].

B. Flow conditions and computational arrangement

A schematic view of the flow configuration investigated is shown in figure 1. A turbulent boundary layer developing over a flat plate is made to interact with an impinging shock. The computational domain extends for $L_x \times L_y \times L_z = 96\,\delta_{in} \times 11.7\,\delta_{in} \times 5.5\,\delta_{in}$, in the streamwise (x), wall-normal (y) and spanwise (z) directions, δ_{in} being the inflow boundary layer thickness. The oblique shock is introduced in the simulation by locally imposing the inviscid Rankine-Hugoniot jump conditions at the top boundary so as to mimic the effect of the shock generator and the nominal shock impingement point is $x_{sh} = 69.5\delta_{in}$, Non-reflecting boundary conditions are enforced at the outflow and at the top boundary, away from the incoming shock. A recycling/rescaling procedure is used for turbulence generation at the inflow plane, whereby staggering in the spanwise direction is used to minimize spurious flow periodicity [29]. The recycling station is placed at $x_{rec} = 48\delta_{in}$, sufficiently distant from the inflow to guarantee proper streamwise decorrelation of the boundary layer statistics [35] and to prevent any spurious low-frequency dynamics associated with the recycling procedure.

5

Test case	Line-style	M_∞	$Re_{\theta 0}$	φ	s	T_w/T_∞	$\mathrm{T}u_\infty/\delta_0$	L/δ_0	L_{sep}/δ_0
BL-s0.5	- - -	2.28	2500	8°	0.5	0.96	218.9	–	–
BL-s1.9	- - -	2.28	2500	8°	1.9	3.66	187.2	–	–
SBLI-s0.5	—•—	2.28	2500	8°	0.5	0.96	598.7	2.90	0.55
SBLI-s0.75	—○—	2.28	2500	8°	0.75	1.44	455.5	3.31	1.67
SBLI-s1.0	——	2.28	2500	8°	1.0	1.93	840.1	3.74	2.11
SBLI-s1.4	—⊞—	2.28	2500	8°	1.4	2.70	669.6	4.32	2.89
SBLI-s1.9	—■—	2.28	2500	8°	1.9	3.66	1002.6	4.97	3.98

TABLE I: Flow parameters for DNS simulations. φ is the incidence angle of shock generator, $s = T_w/T_r$ the wall-to-recovery temperature ratio in the interaction zone, L is the interaction lengthscale, and L_{sep} is the length of the recirculation bubble. The subscript 0 refers to properties taken upstream of the temperature step change at $x_0 = 50\delta_{in}$. T is the time span used for the computation of the flow statistics.

A characteristic wave decomposition is used at the no-slip wall, where perfect reflection of acoustic waves is enforced, and the wall temperature is held fixed. The turbulent boundary layer develops under nominal adiabatic conditions up to $x_T = 54\delta_{in}$ (the wall temperature T_w being equal to the recovery temperature T_r) and local cooling/heating is applied for $x > x_T$ by specifying the wall-to-recovery-temperature ratio $s = T_w/T_r$ to the desired value. To avoid a discontinuity in the wall temperature distribution, a smoothed step change is prescribed according to (see figure 2)

$$T_w(x) = T_r \left[1 + \frac{s-1}{2} \left(1 + \tanh \frac{2(x - x_T)}{\delta_{in}} \right) \right].$$

Five DNS have been carried out at various values of the wall-to-recovery-temperature ratio, spanning cold ($s = 0.5, 0.75$), adiabatic ($s = 1.0$) and hot ($s = 1.4, 1.9$) walls. These cases are labelled as SBLI-s0.5, SBLI-s0.75, SBLI-s1.0, SBLI-s1.4, SBLI-s1.9, respectively. The flow conditions for the various runs are reported in table I. For all cases, the free-stream Mach number is $M_\infty = 2.28$ and the deflection angle of the wedge shock generator is $\varphi = 8°$, corresponding to an overall pressure rise $p_3/p_\infty = 2.46$ and temperature rise $T_3/T_\infty = 1.30$ across the interaction. The Reynolds number of the incoming boundary layer based on the momentum thickness, evaluated at a reference station upstream the temperature step
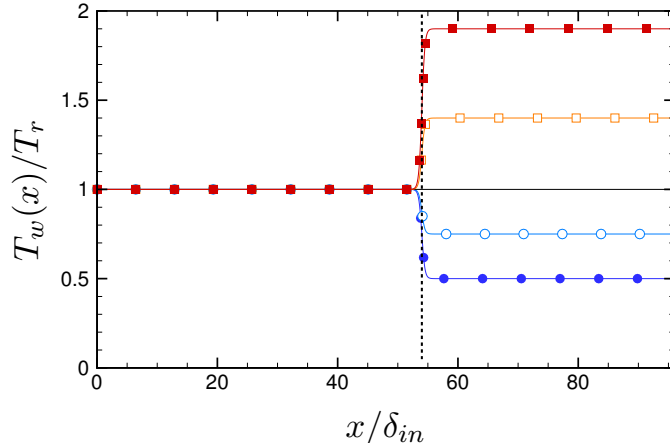
FIG. 2: Distribution of the wall temperature as a function of the longitudinal coordinate. The vertical dotted line denotes the location of the temperature step change. Refer to table I for nomenclature of the DNS data.

change ($x_0 = 50\delta_{in}$) is $Re_{\theta_0} \approx 2500$. For reference purposes, two additional simulations have been also carried out, corresponding to DNS of spatially evolving boundary layers (in the absence of impinging shock) subjected to the same temperature step change as in SBLI-s0.5 and SBLI-s1.9. These two cases are denoted as BL-s0.5 and BL-s1.9, respectively.

The domain is discretized with a mesh consisting of $6144 \times 448 \times 448$ grid nodes, that are uniformly distributed in the spanwise direction. In the streamwise and wall-normal directions stretching functions are employed to better resolve the interaction region and to cluster grid nodes towards the wall. In particular, a hyperbolic sine mapping is applied from the wall $y = 0$ up to $y = 3.5\delta_{in}$. A uniform mesh spacing is then used above this location and an abrupt variation of the metrics is avoided by a suitable smoothing of the connection zone. In terms of wall units (based on the friction velocity u_τ and viscous length-scale δ_v) evaluated in the undisturbed turbulent boundary layer at x_0, the streamwise and spanwise spacings are $\Delta x^+ = 5.9$, $\Delta z^+ = 3.1$; in the wall-normal direction the spacing ranges from $\Delta y^+ = 0.49$ at the wall to $\Delta y^+ = 6.7$ at the edge of the boundary layer. We point out that such mesh spacings are significantly smaller than those usually employed for DNS of SBLI under adiabatic conditions. The motivation is dictated by the need of maintaining adequate resolution even when strong cooling is applied, which is the most challenging case in terms of spacing requirements, due to the drastic reduction of the viscous length-scale.

The simulations have been run on a parallel cluster using 4096 cores, for a total of 7 Mio CPU hours. The time span over which the flow statistics have been computed is reported

7

Run	Re_θ	Re_{δ_2}	Re_τ	H	H_i	$C_f(\cdot 10^3)$
ALL	2410	1509	450	3.64	1.41	2.45

TABLE II: Global properties of the incoming turbulent boundary layer at $x_0 = 50\delta_{in}$. θ denotes the momentum thickness. The Reynolds number are defined as $Re_\theta = \rho_\infty u_\infty \theta/\mu_\infty$; $Re_{\delta_2} = \rho_\infty u_\infty \theta/\overline{\mu}_w$; $Re_\tau = \overline{\rho}_w u_\tau \delta/\overline{\mu}_w$; H and H_i are the compressible and incompressible shape factor, respectively, computed with mean velocity $\overline{u}$. C_f is the skin friction coefficient.

in table I. In the following, the boundary layer thickness in the undisturbed boundary layer at station x_0 is assumed as reference length for all flow cases ($\delta_0 = 1.45\,\delta_{in}$). The results are reported using scaled interaction coordinates $x^* = (x - x_{sh})/\delta_0$, $y^* = y/\delta_0$. For the sake of notational clarity, the streamwise, wall-normal and spanwise velocity components will be hereafter denoted as u, v, w, respectively, and either the Reynolds ($\varphi = \overline{\varphi} + \varphi'$) or the mass-weighted ($\varphi = \widetilde{\varphi} + \varphi''$, $\widetilde{\varphi} = \overline{\rho\varphi}/\overline{\rho}$) decomposition will be used for the generic variable φ.

It is worth pointing out that the flow conditions of case SBLI-s1.0 are essentially identical to that of our previous DNS, reported in Pirozzoli and Bernardini [12], based on the experiment by Piponniau *et al.* [5]. The extensive comparison available in that paper (not repeated here) showed that the global structure of the flow (mean velocities and turbulence velocity fluctuations) predicted by DNS is in very good agreement with that observed in the experiment, provided that the differences in the overall size of the interaction zone are suitably compensated. Indeed, the size of the separation bubble found in the computation is approximately 30% smaller than the experimental one. As later shown by Bermejo-Moreno *et al.* [36] this difference can be ascribed to the assumption of spanwise periodicity applied in the numerical simulation, which avoids confinement effects from lateral walls that are inevitable in the experiment and are known to cause substantial increase of the separation bubble size.
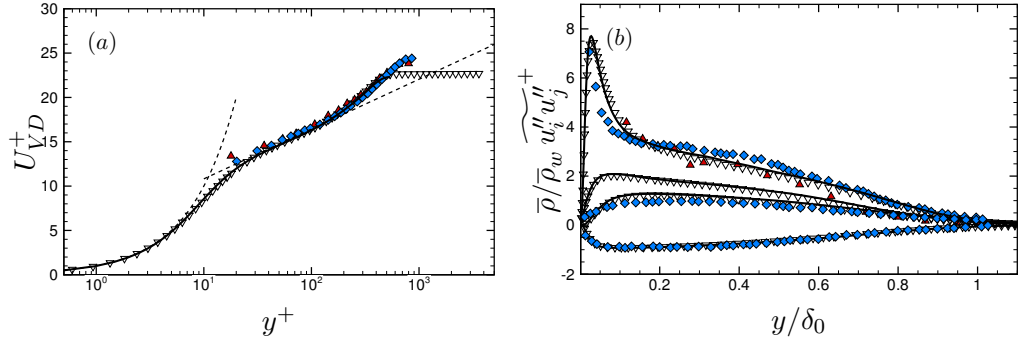
FIG. 3: Comparison of (a) van Driest-transformed mean velocity profile and (b) density-scaled Reynolds stress components at the adiabatic station x_0 with reference numerical and experimental data. Symbols denote experiments by Eléna and Lacharme [37] (triangles, $M_\infty = 2.32$, $Re_\theta = 4700$), Piponniau *et al.* [5], (diamonds, $M_\infty = 2.28$, $Re_\theta = 5100$) and the incompressible DNS data by Schlatter and Örlü [38] (inverted triangles, $Re_\theta = 1410$).
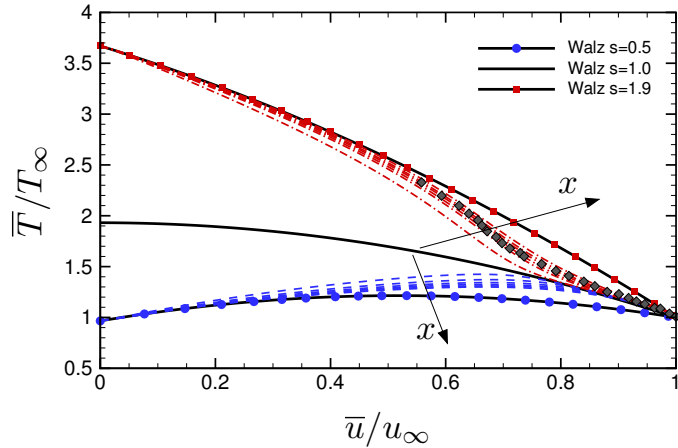

FIG. 4: Distribution of temperature-velocity relationship at various stations for BL-s0.5 and BL-s1.9. Refer to table I for nomenclature of the DNS data. The solid lines indicate the equilibrium solution 1 for cold, adiabatic and hot walls. The black arrows indicate the direction of increasing x. The grey diamonds denote reference experiments with $s = 2$ by Debiève *et al.* [39].

9
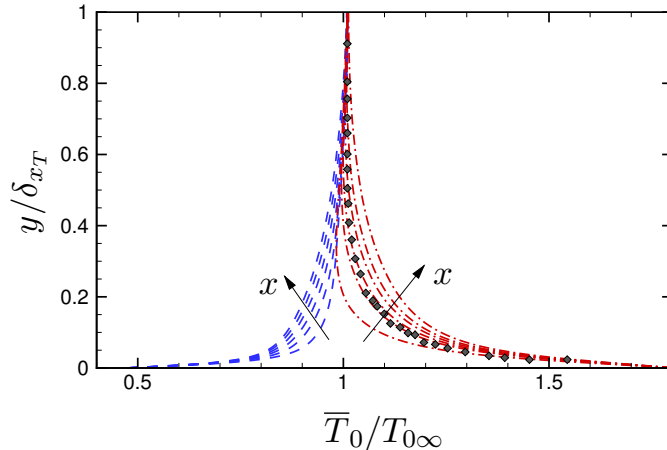
FIG. 5: Distribution of total temperature profiles at various streamwise stations for BL-s0.5 and BL-s1.9. The wall-normal coordinate is normalized through the boundary layer thickness at x_T (δ_{x_T}). Refer to table I for nomenclature of the DNS data. The black arrows indicate the direction of increasing x. The grey diamonds denote reference experiments with $s = 2$ by Debiève *et al.* [39].

III. DNS RESULTS

A. Characterization of the incoming flow

A comparison of the basic velocity statistics of the incoming turbulent boundary layer with reference experiments and numerical simulations is shown in figure 3. The DNS data are taken at the reference station $x_0 = 50\delta_{in}$, which is still in the adiabatic portion of the wall, and where the friction Reynolds number (ratio between the boundary layer thickness and the viscous length-scale) is $Re_\tau \approx 450$. The global properties of the boundary layer at this location are summarized in Table II.

As expected, when the van Driest-transformation $dU_{VD} = (\overline{\rho}/\overline{\rho}_w)^{1/2}d\overline{u}$ is applied to take into account for the variation of the thermodynamic properties through the boundary layer, a collapse with reference low-speed data at comparable Re_τ [38] is observed, and the mean velocity profile exhibits the onset of a small region with a nearly logarithmic behavior. The density-scaled Reynolds stresses, reported in 3b, highlight close similarities with the incompressible distributions and a very good agreement is also obtained with reference compressible experiments, except for the wall-normal velocity variance, which is typically underestimated by measurements.
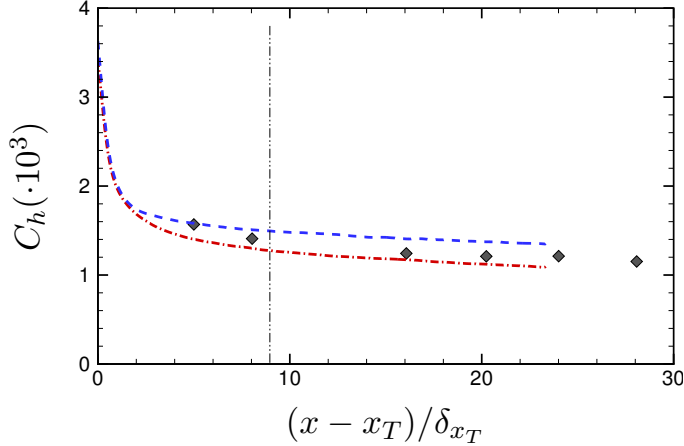
FIG. 6: Distribution of the Stanton number as a function of the streamwise distance from the temperature step change, normalized by the boundary layer thickness at x_T (δ_{x_T}). Refer to table I for nomenclature of the DNS data. The grey diamonds denote reference experiments with $s = 2$ by Debiève *et al.* [39]. The vertical line denotes the impingment shock location for SBLI simulations.

The main effect of the temperature step change on the incoming flow can be understood by looking at figure 4 where the temperature-velocity relationship in the boundary layer is reported for simulations BL-s0.5 and BL-s1.9 at various stations along the streamwise direction, from x_0 to the end of the computational domain. This representation is very suited to describe the adaptation process of the boundary layer to the new thermal conditions at the wall. The shape of the profiles at the various x-stations suggests that the outer region of the boundary layer significantly deviates from the equilibrium Walz solution,

$$\frac{\overline{T}}{T_\infty} = \frac{T_w}{T_\infty} + \frac{T_r - T_w}{T_\infty}\frac{\overline{u}}{u_\infty} + \frac{T_\infty - T_r}{T_\infty}\left(\frac{\overline{u}}{u_\infty}\right)^2 \;,\quad T_r = T_\infty + r\frac{u_\infty^2}{2\,C_p}, r = (Pr)^{1/3}, \quad (1)$$

and even at the end of the computational domain the recovery process is not yet completed for either of the cold or hot wall cases. A similar conclusion was also reported by Debiève *et al.* [39], who investigated the effect of heating by considering a step change in the wall temperature distribution of a spatially evolving supersonic turbulent boundary layer at freestream Mach number $M_\infty = 2.3$, wall-to-recovery temperature ratio $s = 2$ and Reynolds number based on the momentum thickness at the temperature step change $Re_\theta = 4100$. Their data, taken 8 boundary layer thicknesses downstream the beginning of the heated wall, are also included in figure 4. The close agreement between the experimental measurements, and the DNS profile at the corresponding location provides a confirmation of the quality of

11

the present simulations with non-adiabatic wall conditions.

A further comparison is shown in figure 5, where the distribution of the total temperature in the boundary layer is shown. The figure allows to appreciate the rapid growth of the thermal boundary layer starting from the step change position and again highlights a remarkable agreement between the experimental measurements and DNS data, despite the slightly different nominal conditions in the wall temperature and Reynolds number.

To highlight the effect of heating/cooling on the heat transfer rate, the spatial distribution of the Stanton number

$$C_h = \frac{q_w}{\rho_\infty \, u_\infty C_p \, (T_w - T_r)} \ , \quad q_w = -k \left. \frac{\mathrm{d}\overline{T}}{\mathrm{d}y} \right|_w$$

is shown in figure 6, where the origin of the streamwise coordinate is located at the beginning of the step change (x_T). For both cooling and heating, the simulation predicts a rapid decay of the heat transfer coefficient towards values typical of an equilibrium boundary layer, and in agreement with recent DNS data [40], C_h is found to increase when s decreases. In this case the agreement with the experimental data (available for the hot wall) is reasonably good, the computed values being approximately 8% lower than the measurements. These differences might be explained recalling that in the experiment C_h was computed through an iterative procedure based on the theoretical Walz's temperature-velocity relationship, which is far from being valid past the step change location, as previously seen in figure 5.

B. Effect of wall temperature on SBLI flow fields

To provide an overview of the flow organization and a qualitative perception of the influence of the wall thermal conditions, we report in figure 7 contours of mean velocity components and of mean density gradient magnitude for some representative values of s (0.5, 1 and 1.9). The typical topology of SBLI is observed for all flow cases, independently of the wall temperature: (i) the incoming turbulent boundary layer thickens within the interaction region and relaxes to a new equilibrium state further downstream; (ii) a compression fan develops near the separation point well upstream of the nominal impinging location; (iii) away from the wall the compression waves coalesce to form the principal reflected shock; and (iv) the flow turns through an expansion fan towards the wall and reattaches.

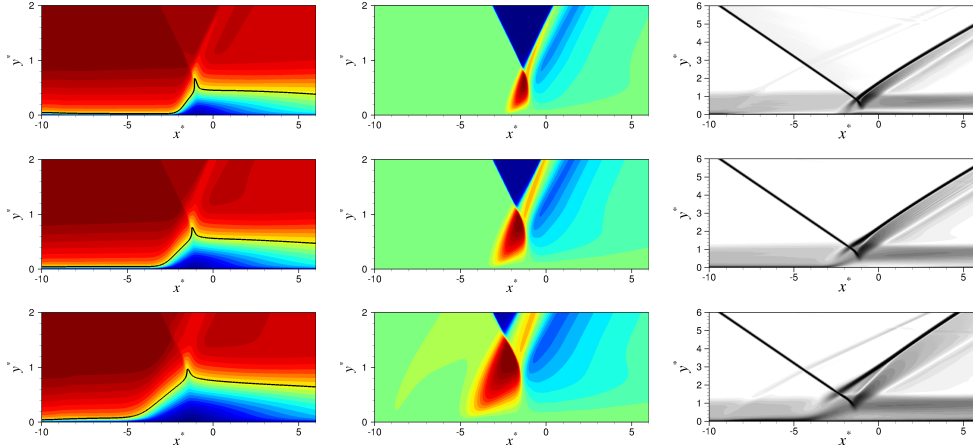Snapshots of the instantaneous density field and of its wall-normal derivative (numerical

FIG. 7: Contours of mean streamwise velocity (left panels), vertical velocity (middle panels) and magnitude of the mean density gradient (right panels) at various wall-to-recovery-temperature ratios, increasing from top to bottom ($s = 0.5, 1, 1.9$). The black line denotes the sonic line. Twenty-four contour levels are shown in the range: $0 < \overline{u}/u_\infty < 1$; $-0.13 < \overline{v}/u_\infty < 0.13$; $0 < e^{-|\nabla\overline{\rho}|/\rho_\infty} < 1$.
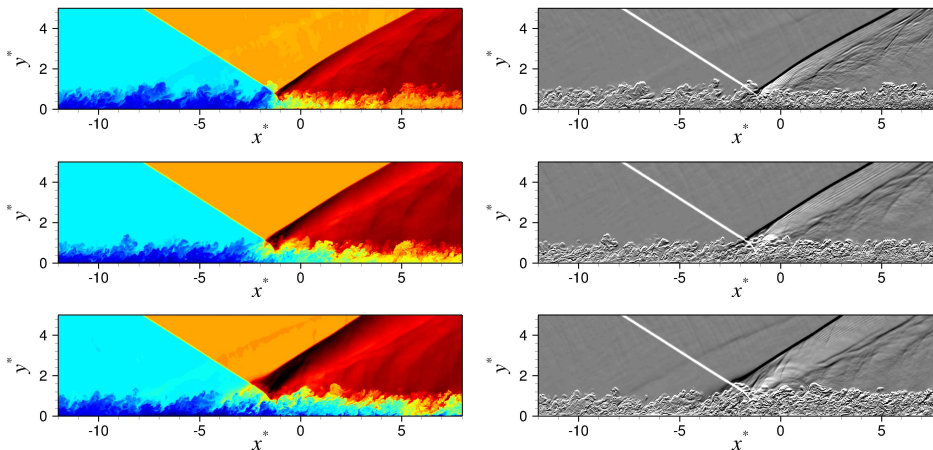
FIG. 8: Contours of instantaneous density (left panels) and wall-normal density gradient (right panels) in the longitudinal mid-plane at various wall-to-recovery-temperature ratios, increasing from top to bottom ($s = 0.5, 1, 1.9$). Sixty-four contour levels are shown in the range: $0.48 < \rho/\rho_\infty < 2.12$; $-1.5 < \mathrm{d}\rho/\mathrm{d}y/\rho_\infty < 1.5$.

schlieren) in the longitudinal mid-plane are reported in figure 8. These visualizations bring to light the convoluted structures of the turbulent boundary layer and allow to appreciate the complex pattern of waves originating from the interaction with the impinging shock. The step change imposed in the wall temperature distribution is also revealed in figure 8
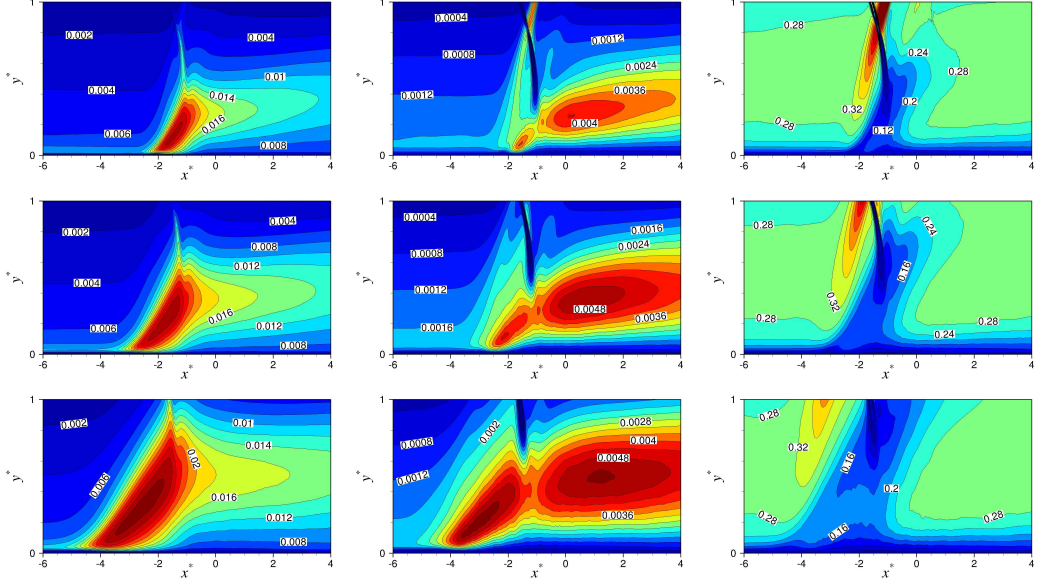
13

FIG. 9: Contours of turbulence kinetic energy k/u_∞^2 (left panels), Reynolds shear stress $\widetilde{u''v''}/u_\infty^2$ (middle panels) and structure parameter Π (right panels) at various wall-to-recovery-temperature ratios, increasing from top to bottom ($s = 0.5, 1, 1.9$).

by the formation of a weak disturbance originated at $x^* \approx -9$, also visible in the mean density gradient of figure 7. The main effect of the wall thermal condition is a change in the interaction scales, well highlighted by the mean and instantaneous visualizations, that clearly shows that the impinging shock penetrates deeper in the incoming turbulent boundary layer when the wall temperature is reduced. This effect is mainly associated with the displacement of the sonic line (displayed in 7) towards to (away from) the wall with wall cooling (heating). The interaction length-scale L (see table I), defined as the distance between the nominal incoming shock impingement point and the apparent origin of the reflected shock, is strongly affected by s. Compared to the adiabatic case, L decreases (increases) significantly with wall cooling (heating), in agreement with previous experimental findings for impinging shock and compression ramp configurations [18, 21].

A strong amplification of turbulence kinetic energy $k = \widetilde{u_i''u_i''}/2$ and Reynolds shear stress $\widetilde{u''v''}$ is found across the interaction region, as revealed by figure 9. For all SBLI cases, a remarkable growth is observed in the first part of the interaction and the maximum values of both k and $\widetilde{u''v''}$ are seen to gradually detach from the wall. This behavior is associated with the development of a shear layer at the separation shock and is consistent with previous numerical and experimental findings in supersonic [4, 20] and transonic interactions [29]. To
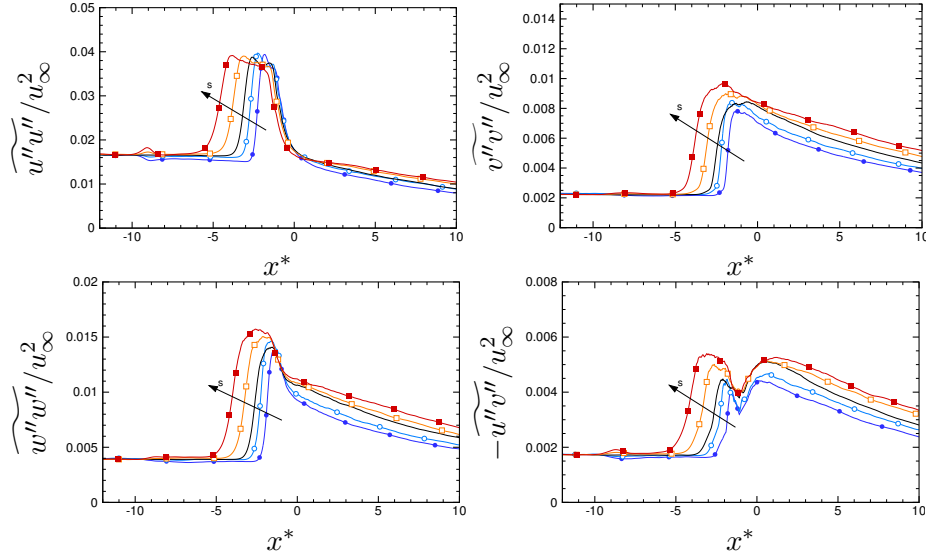
14

FIG. 10: Streamwise sistribution of the peaks of the Reynolds stress components for the various SBLI flow cases. Refer to table I for nomenclature of the DNS data.

characterize the behavior of turbulence across the interaction, the ratio between the absolute value of the shear stress and the turbulence kinetic energy, known as structure parameter (Π), is also reported in figure 9. In the upstream region this quantity is approximately constant for all cases, assuming a value typical of a turbulent boundary layer not too far from the equilibrium ($\Pi \approx 0.3$). At the beginning of the interaction, independently of s, a rapid decrease is observed and Π attains values in the range $0.1 \div 0.15$, before gradually recovering the original value. The influence of the wall temperature on the behavior of the structure parameter is found to be marginal, except for the previously mentioned shrinking/expansion effect of the interaction domain.

To better quantify the enhancement of turbulence across the interaction, we have computed at each x station the peak values of the Reynolds stress components, reported in figure 10 as a function of the scaled streamwise coordinate. The distributions are strongly influenced by the wall temperature, an increment of s implying an upstream shift of the turbulence amplification location. Furthermore, the intensity of all the Reynolds stress components is seen to increase when the wall is heated, with the exception of $\widetilde{u''u''}$, whose peak is identical for the various SBLI cases. The maximum amplification (approximately a factor 4 with respect to the upstream level) is attained by the wall-normal component $\widetilde{v''v''}$, whose behavior is qualitatively similar to that of $\widetilde{w''w''}$, whereas the shear stress displays a
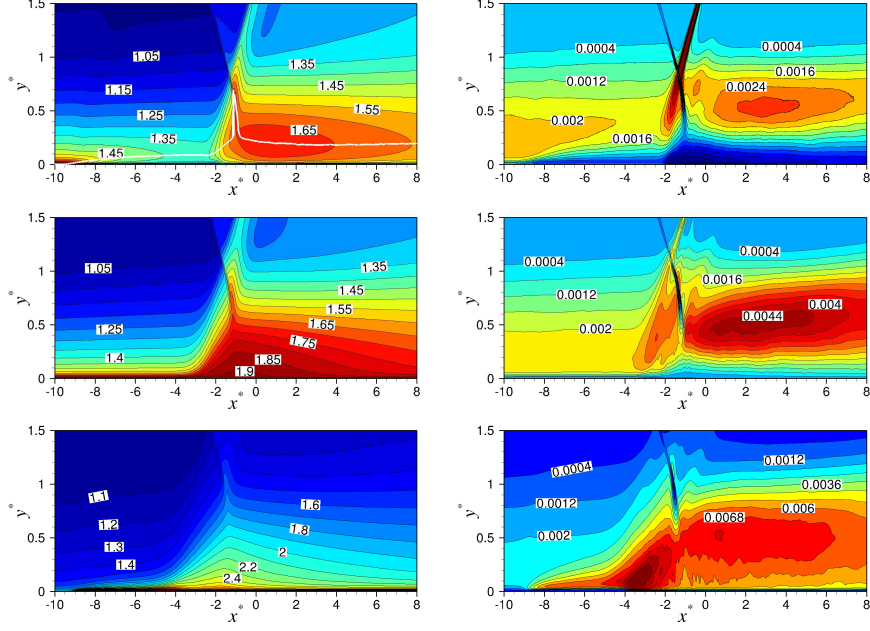
15

FIG. 11: Contours of mean temperature $\widetilde{T}/T_\infty$ (left panels), and wall-normal turbulent heat flux $\widetilde{v''T''}/u_\infty T_\infty$ (right panels) at various s, increasing from top to bottom $(s = 0.5, 1, 1.9)$.

second maximum immediately past the nominal impingment location. We point out that the different amplification undergone by the individual components of the Reynolds stress tensor causes a large increase in the anisotropy across the interaction region, which is a typical feature of this kind of interacting flows previously noticed in experiments [3] and numerical simulations [29].

A major effect of the cooling/heating is found in the fields of the mean temperature $\widetilde{T}$ and of the wall-normal turbulent heat-flux $\widetilde{v''T''}$, displayed in figure 9, where the y-axis has been magnified to better highlight the near-wall behavior. The impinging shock greatly affects both $\widetilde{T}$ and $\widetilde{v''T''}$, leading to a thickening of the thermal boundary layer and to a strong amplification of the turbulent heat flux. However, the specific behavior of the flow significantly depends on the wall thermal condition. In particular, in both the adiabatic and hot wall case the mean temperature attains its maximum at the wall and a positive correlation is always found between temperature and wall-normal velocity fluctuations across the interaction region. On the other hand, when surface cooling is applied, a local maximum of the mean temperature within the boundary layer starts to develop (white solid line in figure 9a) , which moves far away from the wall at the beginning of the interaction process.
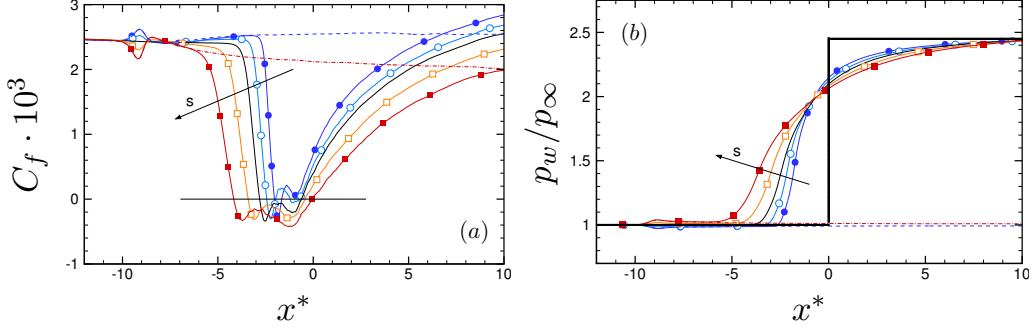
16

FIG. 12: Distribution of (a) skin friction coefficient and (b) mean wall pressure at various wall-to-recovery-temperature ratios. Refer to table I for nomenclature of the DNS data. The dotted line denotes the pressure jump predicted by the inviscid theory.
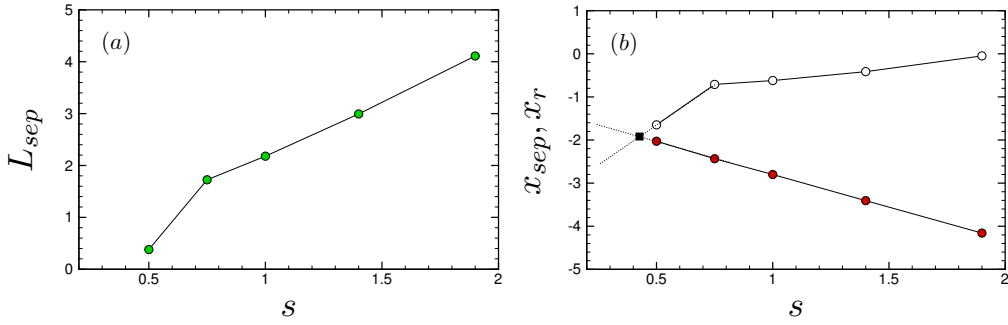

FIG. 13: Distribution of (a) mean separation length L_{sep} and (b) location of the separation (x_{sep}, solid circles) and reattachment (x_r, open circles) points as a function of the wall-to-recovery temperature ratio. The black square is the extrapolated point corresponding to the condition of incipient separation.

In this case, a negative $\widetilde{v''T''}$ correlation is found close to the wall, and as observed for a cold spatially evolving boundary layer [40], the crossover position ($\widetilde{v''T''} = 0$) occurs close to the location of maximum mean temperature.

C. Wall properties in adiabatic and non-adiabatic SBLI

The spatial distribution of the mean skin friction coefficient $C_f = 2\tau_w/\rho_\infty u_\infty^2$ at various s is depicted in figure 12(a). For reference purposes, we also report in the figure the skin friction distribution of the cold and hot spatially evolving boundary layers BL-s0.5 and BL-s1.9 (dashed lines). Upstream of the region of shock influence, a collapse of the curves for the same temperature conditions is observed. The temperature step change produces an
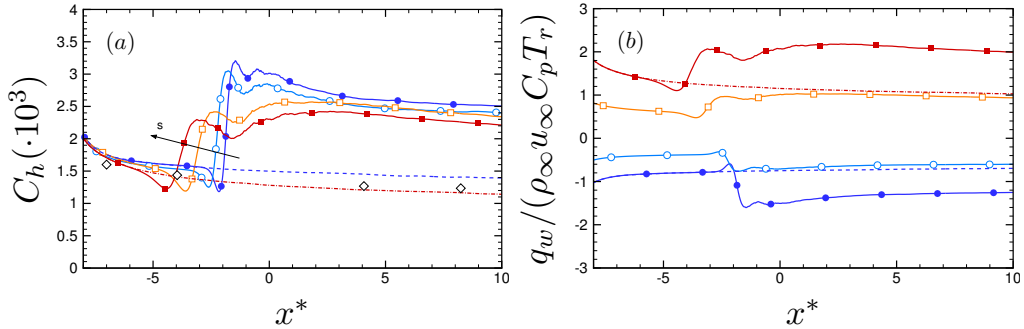
FIG. 14: Distribution of (a) Stanton number and (b) wall heat flux at various wall-to-recovery-temperature ratios. Refer to table I for nomenclature of the DNS data. Open diamonds denote reference experiments with $s = 2$ by Debiève *et al.* [39].

abrupt variation of the skin friction, characterized by a maximum (minimum) when cooling (heating) the wall. In the absence of the shock the skin friction distribution gradually relaxes to that of an equilibrium boundary layer, and in agreement with previous studies [40], C_f is increased by wall cooling and decreased by heating. In the presence of the impinging shock, the skin friction exhibits a sharp decrease at the beginning of the interaction and for all cases mean flow separation is observed. The extent of the recirculation region (L_{sep}) is reported in table I and plotted in figure 13, where the location of the separation and reattachment points is also shown. Compared to the adiabatic case, wall cooling results in a significant reduction of L_{sep} (-74% for SBLI-s0.5), whereas heating the wall leads to the opposite effect ($+79.8\%$ for SBLI-s1.9). The location of the separation point is most affected by the wall temperature change, whereas the boundary layer reattachment is less influenced by s, being mainly controlled by the nominal (fixed) impinging shock location. A simple extrapolation of the available data leads to a value of $s = 0.427$ to obtain the condition of incipient separation. We observe that, for all cases, the skin friction in the interaction region exhibits the typical W-shape previously observed in both laminar and (adiabatic) turbulent shock boundary layer interactions [12, 41], characterized by two minima, which are both affected by s. In particular, an increase of the wall-to-recovery-temperature ratio produces an upstream displacement of the first minimum, associated with the upstream shift of the separation shock. The location of the second minimum is relatively insensitive to s but its magnitude decreases when the wall temperature is raised.

The major influence of cooling/heating is also apparent from the mean wall pressure p_w, whose distribution is reported in figure 12(b). Heating the wall shifts upstream the
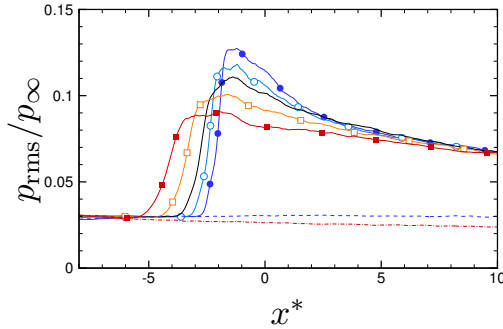
FIG. 15: Distribution of root-mean-square wall pressure at various wall-to-recovery-temperature ratios. Refer to table I for nomenclature of the DNS data.

beginning of the interaction, leading to a smoother pressure rise. The opposite behavior occurs in the case of cooling, that produces a downstream shift of the upstream influence and a steeper variation of p_w within the interaction zone. Interestingly, all the curves cross at the same point ($x^* = -1$) close to the nominal impingment location, before gradually relaxing towards the value predicted by the inviscid theory. In the downstream portion, contrary to some experimental observations [20], our data do not show any overshoot with respect to the level of the inviscid fluid solution.

To characterize the heat transfer behavior across the interaction the spatial distribution of the Stanton number C_h is reported in figure 14 (a), for all flow cases (BL and SBLI) here investigated. As a reference purpose, we also show in figure 14 (b) the wall heat flux q_w, that being normalized by the constant factor ($\rho_\infty u_\infty C_p T_r$), provides a perception of the direction and of the effective amount of heat exchanged at the wall in the various cases. A strong amplification of the heat transfer rate C_h is found in the interaction region with respect to the reference cooled/heated boundary layers, with a maximum increase of approximately a factor 2 for the cooled and 1.7 for the heated wall. A complex variation of the Stanton distribution is observed when varying the wall thermal condition, the curves being characterized by four local extrema. First, St decreases attaining a minimum in the proximity of the separation point, followed by a sharp increase in the interaction zone, with the peak achieved at the same point where the skin friction features its local maximum. In the case of heated wall, characterized by an extended separation, the Stanton number exhibits a curvature change with a second minimum around the reattachment point and then increases again attaining a second broad maximum in the downstream relaxation region. In the presence of cold wall, where the extent of the separation bubble is strongly reduced, the curvature change
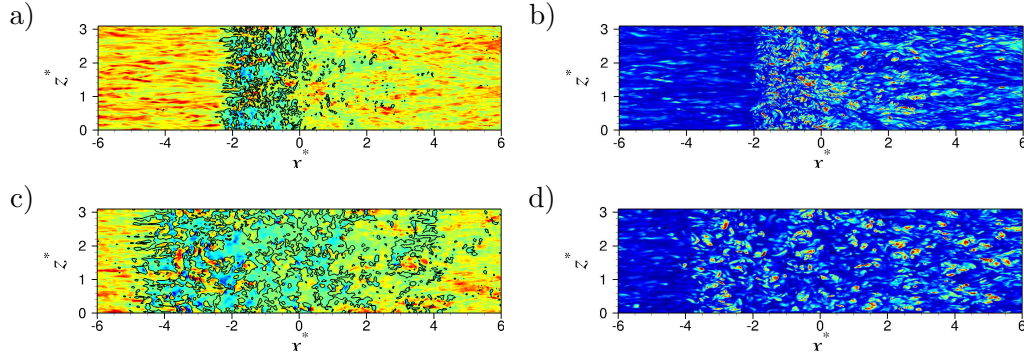
19

FIG. 16: Contours of (a-c) instantaneous skin friction and (b-d) Stanton number for flow
cases SBLI-s0.5 (top panels) and SBLI-s1.9 (bottom panels).

is still observed but St peaks immediately past the reattachment point. These trends are very similar to those reported by Hayashi *et al.* [22], who explored the effect of the shock strength (by varying the shock generator wedge angle) under the same thermal condition (cold wall). In particular, the Stanton number distribution found in the experiments for strong interactions is here recovered by increasing the wall-to-recovery-temperature ratio.

We remark that, despite the fact that wall cooling results in a weaker interaction (as far as the separation bubble size is concerned), the reduction of the length-scales in the streamwise and wall normal direction produces stronger temperature gradients at the wall thus leading to larger heating rates. Similarly, since the shock penetrates deeper in the boundary layer and the pressure jump imparted by the shock must be sustained in a narrower region, cooling the wall increases the root-mean-square wall pressure p_{rms}, as shown in figure 15. The location of the maximum values of p_{rms} perfectly matches that of the first peak in the Stanton distribution, implying that the generation of high thermal loads is likely to be associated with the turbulence amplification in the interaction region.

The results on the mean skin friction and the Stanton number reported in the previous figures confirm the experimental observations of Schülein [23], who highlighted that the analogy between momentum and heat transfer, which is well assessed in equilibrium flows and represents the basis of many simplified physical models is not valid in the interaction region. This conclusion is not surprising, since even the most advanced and refined forms of the Reynolds analogy [42, 43] are all based on the chief assumption/approximation of a quasi-one-dimensional flow, which clearly fails in the presence of mean flow separation as in the present SBLI cases.
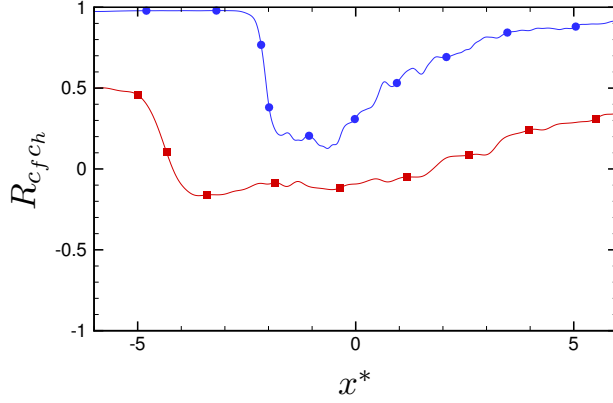
FIG. 17: Distribution of the correlation coefficient between c_f and c_h for flow cases SBLI-s0.5 (blue line with circles) and SBLI-s1.9 (red line with squares)

.

To examine in depth the relationship between momentum and heat transfer, and to better characterize the unsteady behavior of the flow we show in figure 16 contours of the instantaneous skin friction c_f and instantaneous heat transfer coefficient c_h in the wall plane, for the two extreme cases SBLIs-0.5 and SBLIs-1.9. We also provide more quantitative information in figure 17 by reporting their correlation coefficient $(R_{c_f c_h})$, as a function of the streamwise coordinate. Upstream of the interaction, a streaky pattern typical of a zero-pressure-gradient boundary layer is found for c_f and c_h in both the cold and hot wall cases. This region is characterized by a positive correlation between the fluctuating friction and heat transfer coefficients, especially in the case of cooling $(R_{c_f c_h} = 0.98)$. This scenario completely changes across the interaction, where flow patches of instantaneously reversed flow are found, starting from the beginning of the interaction and extending well into the recovery zone. In this region the local Stanton number exhibits a strong intermittent behavior, characterized by scattered spots with extremely high heat transfer rates and the correlation coefficient displays a rapid decay, attaining a nearly flat distribution throughout the separation bubble. The relaxation region is characterized by a gradual recover of the upstream behavior which is not yet completed at the end of the computational domain.

To further characterize the flow unsteadiness and to assess the possible influence of the reflected shock motion on the wall heat flux, we report in figure 18 the pre-multiplied spectra of both the wall pressure and the instantaneous heat flux as a function of Strouhal number $St = f \delta_0 / u_\infty$ and streamwise position x^*. The spectral maps refer to SBLIs1.9, which is characterized by extended separation and correspond to the flow case for which
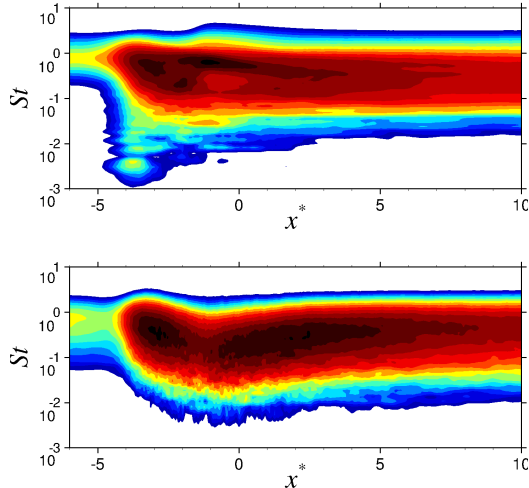
FIG. 18: Contours of pre-multiplied (a) pressure and (b) heat flux spectra ($f\,E(f)$) for flow case SBLI-s1.9 as a function of streamwise location and Strouhal number.

the low-frequency shock motion is more evident. The power spectral densities have been computed using the Welch method, subdividing the overall pressure record into 4 segments with 50% overlapping, which are individually Fourier-transformed. The frequency spectra are then obtained by averaging the periodograms of the various segments, which allows to minimize the variance of the PSD estimator, and by applying a Konno-Omachi smoothing filter [44] that ensures a constant bandwidth on a logarithmic scale. The map of the wall pressure signal shows the typical features observed in previous studies [15]. Upstream of the interaction zone the spectra are bump-shaped as for canonical wall-bounded flows, with a peak at St $\sim O(1)$, associated with the energetic turbulent structures of the boundary layer. A similar shape is also found in the downstream relaxation region, although the spectral density is broadened and the peak shifted to lower frequencies owing to the thicknening of the boundary layer. A different behavior is observed at the beginning of the interaction region, close to the foot of the reflected shock, where a broad peak appears in the map at low frequencies, centered at $St \approx 0.004$, corresponding to a Strouhal number based on the separation length $St_L = fL_{sep}/u_\infty \approx 0.025$. This secondary peak is the signature of the broadband motion of the reflect shock, that in SBLI with massive separation is known to be mainly driven by a donwstream mechanism associated with the dynamics of the separation bubble [5, 16].

The power spectral density of the heat transfer coefficient brings to light a completely

different picture. In this case no evidence of any low frequency dynamics is apparent and most part of the energy is contained at intermediate/high frequencies throughout the interaction. In particular a strong amplification of the heat transfer fluctuations is found close to the separation and reattachement points, with a shift toward intermediate frequencies, classically associated with the shedding of vortical structures in the shear layer that develops in the first part of the interaction [14]. This again suggests that in the flow cases here investigated, the primary mechanism responsible for the generation of peak heating in the interaction zone is the turbulence amplification associated with the SBLI.

IV. CONCLUSIONS

In the present work the influence of different wall thermal conditions on the properties of impinging shock-wave/turbulent boundary layer interactions is investigated by means of direct numerical simulations at $M_\infty = 2.28$ and shock angle $\varphi = 8°$. Five different values of wall-to-recovery-temperature ratio are considered, corresponding to cold ($s = 0.5, 0.75$), adiabatic ($s = 1$) and hot ($s = 1.4, 1.9$) walls. The characteristic features of SBLI are observed for all flow cases, but the interaction properties are significantly affected by the wall temperature and our results confirm the observations of the few experimental data available in literature. Wall cooling has some beneficial effects on SBLI, leading to a considerable reduction of the interaction scales and size of the separation bubble, whereas the opposite holds for wall heating. A complex spatial variation of the Stanton number is found across the interaction, whose structure strongly depends on the wall-to-recovery-temperature ratio. The fluctuating heat flux exhibits a strong intermittent behavior, characterized by scattered spots with extremely high values compared to the mean, and the analogy between momentum and heat transfer typical of equilirium boundary layers is no longer valid in the interaction region. The pre-multiplied spectra of the Stanton number do not show any evidence of the influence of the low-frequency shock motion, and the primary mechanism for the generation of peak heating is found to be linked with the turbulence amplification in the interaction region.

If the primary objective is to reduce flow separation, our results indicate that wall cooling can be considered as an effective method for flow control. However, since the pressure jump imparted by the shock must be sustained by the boundary layer in a narrower region, when

the wall temperature decreases, the maximum values of thermal (heat transfer rates) and dynamic loads (root-mean-square wall pressure) are found in the case of a cold wall.

We expect that the DNS database developed in this work, with statistics and raw data available at `http://newton.dima.uniroma1.it/osbli/`, would be useful for the high-speed turbulence modeling community, by fostering the development of advanced models to improve the prediction of heat transfer in SBLI. Future efforts will be made to extend our database to a wider range of flow conditions, including different Mach numbers and shock strengths.

ACKNOWLEDGMENTS

---

[1] D. S. Dolling, AIAA J. **39**, 1517 (2001).

[2] D. Dolling and M. Murphy, AIAA J. **21**, 1628 (1983).

[3] J. Délery and J. Marvin, *Shock-wave boundary layer interactions*, AGARDograph 280 (DTIC Document, 1986).

[4] P. Dupont, C. Haddad, and J. Debiève, J. Fluid Mech. **559**, 255 (2006).

[5] S. Piponniau, J. Dussauge, J. Debiève, and P. Dupont, J. Fluid Mech. **629**, 87 (2009).

[6] R. Humble, G. Elsinga, F. Scarano, and B. van Oudheusden, J. Fluid Mech. **635**, 47 (2009).

[7] L. Souverein, P. Dupont, J. F. Debiève, J. P. Dussauge, B. W. van Oudheusden, and F. Scarano, AIAA J. **48**, 1480 (2010).

[8] N. Adams, J. Fluid Mech. **420**, 47 (2000).

[9] M. Wu and M. Martin, AIAA J. **45**, 879 (2007).

[10] S. Priebe, M. Wu, and M. Martin, AIAA J. **47**, 1173 (2009).

[11] E. Touber and N. Sandham, Theor. Comput. Fluid Dyn. **23**, 79 (2009).

[12] S. Pirozzoli and M. Bernardini, AIAA J. **49**, 1307 (2011).

[13] M. Grilli, P. Schmid, S. Hickel, and N. Adams, J. Fluid Mech. **700**, 16 (2012).

[14] G. Aubard, X. Gloerfelt, and J. Robinet, AIAA J. **51**, 2395 (2013).

[15] B. Morgan, K. Duraisamy, N. Nguyen, S. Kawai, and S. Lele, J. Fluid Mech. **729**, 231 (2013).

[16] N. Clemens and V. Narayanaswamy, Annu. Rev. Fluid Mech. **46**, 469 (2014).

[17] J. Delery, Prog. Aerosp. Sci. **22**, 209 (1985).

[18] F. Spaid and J. Frishett, AIAA J. **10**, 915 (1972).

[19] L. Back and R. Cuffel, AIAA J. **14**, 526 (1976).

[20] J. Delery, La Recherche Aerospatiale **1**, 1 (1992).

[21] V. Jaunet, J. Debiéve, and P. Dupont, AIAA J. **52**, 2524 (2014).

[22] M. Hayashi, A. Sakurai, and S. Aso, NASA TM-77958 **57**, 455 (1986).

[23] E. Schülein, AIAA journal **44**, 1732 (2006).

[24] T. Evans and A. Smits, Exp. Thermal Fluid Sci. **12**, 87 (1996).

[25] A. Hadjadj, AIAA J **50**, 2919 (2012).

[26] J. Nichols, J. Larsson, M. Bernardini, and S. Pirozzoli, Theoretical and Computational Fluid Dynamics , 1 (2016).

[27] N. Fedorova, I. Fedorchenko, and E. Schülein, Computational Fluid Dynamics Journal **10**, 390 (2001).

[28] D. Knight, H. Yan, A. G. Panaras, and A. Zheltovodov, Progress in Aerospace Sciences **39**, 121 (2003).

[29] S. Pirozzoli, M. Bernardini, and F. Grasso, J. Fluid Mech. **657**, 361 (2010).

[30] S. Pirozzoli and M. Bernardini, J. Fluid Mech. **688**, 120 (2011).

[31] F. Ducros, V. Ferrand, F. Nicoud, D. Darracq, C. Gacherieu, and T. Poinsot, J. Comput. Phys. **152**, 517549 (1999).

[32] C. Kennedy and A. Gruber, J. Comput. Phys. **227**, 1676 (2008).

[33] S. Pirozzoli, J. Comput. Phys. **229**, 7180 (2010).

[34] M. Bernardini and S. Pirozzoli, J. Comput. Phys. **228**, 4182 (2009).

[35] M. Simens, J. Jiménez, S. Hoyas, and Y. Mizuno, J. Comput. Phys. **228**, 4218 (2009).

[36] I. Bermejo-Moreno, L. Campo, J. Larsson, J. Bodart, D. Helmer, and J. Eaton, J. Fluid Mech. **758**, 5 (2014).

[37] M. Eléna and J. Lacharme, J. Méc. Théor. Appl. **7**, 175 (1988).

[38] P. Schlatter and R. Örlü, J. Fluid Mech. **659**, 116 (2010).

[39] J. Debiève, P. Dupont, D. Smith, and A. Smits, AIAA J. **35**, 51 (1997).

[40] A. Hadjadj, O. Ben-Nasr, M. Shadloo, and A. Chaudhuri, Int. J. Heat Mass Transfer **81**, 426 (2015).

[41] Katzer, E., J. Fluid Mech. **206**, 477 (1989).

[42] L. Duan, I. Beekman, and M. Martin, J. Fluid Mech. **655**, 419 (2010).

[43] Y. Zhang, W. Bi, F. Hussain, and Z. She, J. Fluid Mech. **739**, 392 (2014).

[44] K. Konno and T. Ohmachi, Bulletin of the Seismological Society of America **88**, 228 (1998).